THE ROYAL SOCIETY

Diffraction topography using white X-ray beams with low effective divergence

By José Baruchel[1], Peter Cloetens[1], Jürgen Härtwig[1] and Michel Schlenker[2]

[1]*European Synchrotron Radiation Facility, BP 220, 38043 Grenoble, France*
[2]*Laboratoire Louis Néel, CNRS, BP 166, 38042 Grenoble, France*

The divergence of the incident X-ray beam as seen from a point in the specimen, the effective divergence α, is of the order of a microradian at a third generation synchrotron radiation source. This entails two effects on white-beam X-ray diffraction topography.

1. The specimen-detector distance can be varied at will in the metre range without appreciable blurring of the image. Thus the discontinuous change in distortion associated with magnetic domains, or implanted layers in a piezoelectric material, can often be directly measured. It was also possible to observe focusing effect due to continuous spatial variations of lattice plane orientation. This effect was visualized in the cases of the images of single dislocations, from elastic resonance patterns, and on wafer-bonded samples.

2. The small value of α can also be described as yielding appreciable lateral coherence of the beam. Propagation of the diffracted beam, i.e. Fresnel diffraction, can turn variations of the phase of the diffracted beam into changes in intensity, hence contrast. In the case of a periodic spatial variation of the phase due to periodic poling, the Talbot effect in the diffracted beam provides the possibility of measuring the difference in phase of a structure factor in inversion-related domains, i.e. for Friedel pairs.

Keywords: X-ray imaging; X-ray topography; synchrotron radiation; Bragg-diffraction imaging; optical coherence; crystallographic phase determination

1. Introduction

In a pioneering paper, Lang *et al.* (1987) explored the optical consequences of the small size, in one dimension, of the synchrotron radiation source at SERC, Daresbury. At third-generation synchrotron radiation (SR) facilities, such as the European Synchrotron Radiation Facility (ESRF, Grenoble, France), the source is small in both directions. This provides new experimental possibilities in X-ray diffraction topography. Some of them are straightforward: the availability of high energy (50–120 keV) photons allows the investigation of heavy and/or bulky samples in transmission, and the photon flux makes real-time experiments on the 10^{-2}–10^{-1} s time-scale feasible (Baruchel *et al.* 1994; Baruchel 1996). This paper delves into the consequences of another feature of such SR facilities, the small angular size of the source as seen from

a point of the sample, or effective divergence of the incident beam, $\alpha = s/D$ ($\approx 10^{-6}$). It is due both to the very small electron beam cross-section dimensions ($s \approx 0.1$ mm) the machine engineers have achieved, and to the large source–specimen distances D used, especially at long beamlines such as ID19. Details in the topographs can be observed with acceptable blurring at a sample-to-detector distance L of the order of 1 m, the geometrical resolution remaining below 1 μm. This allows the use of the crystal-to-detector distance as a new parameter to characterize domains and defects. The fact that α is small is also associated with a high degree of coherence of the X-ray beam. This is already increasingly used in simple transmission for phase radiography and tomography (Baruchel 1996; Cloetens *et al*. 1996, 1997*b*, 1999; Mancini *et al*. 1998; Raven *et al*. 1996; Snigirev *et al*. 1995), but it also provides enhanced possibilities for diffraction topographic work. Thus it becomes necessary, when analysing the contrast observed on topographs, to take into account not only the interaction of the incident beam with the crystal and the propagation of wave-fields within the crystal, but also the propagation of the beam outside the crystal.

The present paper describes examples of diffraction topographic work where the small angular size of the source is a crucial ingredient. They can be divided into two subgroups. The experiments belonging to the first one rest on the angular deviations of the diffracted beams, without interference between them. The second subgroup use the coherence properties of the beam. All these experiments were performed in the white-beam mode. Most of them were carried out at the long (145 m) 'Topography/Imaging' beamline ID19 of the ESRF, the remaining ones being performed at the 'Optics' BM5 beamline.

2. Focusing-related experiments

In most of the published contrast-mechanism models, the relevant information is the distribution of diffracted intensity on the exit face of the crystal, and propagation of the incoming beam to the crystal and of the diffracted beam from the crystal to the detector is ignored. Distortions in a crystal imply misorientations, which can often be visualized and measured by recording white-beam diffraction images at several distances, provided no significant blurring occurs. The present section is devoted to the use of this information in cases where interference does not occur between the various parts of the diffracted beam because they are mutually incoherent. As mentioned in § 1, a rather large value of L (1 m, as compared with a few millimetres in Lang's method, and *ca.* 10 cm on the previous SR topographic set-ups) involves no substantial geometrical degradation of the image when working at the ID19 ESRF beamline. This allows the observation of the broadening (or shrinking) of the image resulting from the distortions of the crystal itself.

Four examples are presented, the first two being performed using projection topographs (extended beam topographs), whereas the last two are based on section topographs (limited beam topographs), which also benefit from observation as a function of the crystal-to-detector distance.

(*a*) *Complete determination of the Burgers vector of an edge dislocation*

Tanner and co-workers demonstrated, more than 20 years ago (Tanner *et al*. 1977), that, when using a SR source where resolution is not limited by the effective incident

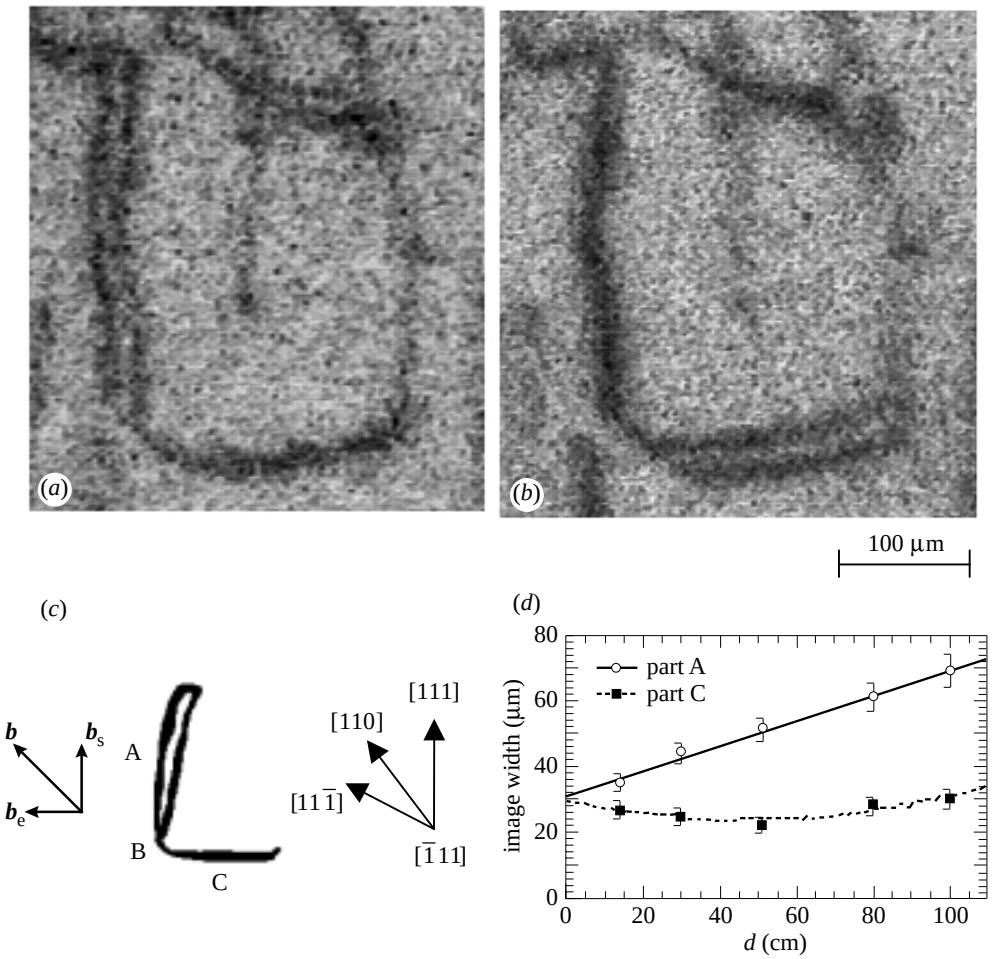

Figure 1. (*a*), (*b*) Contrast change from single to double is observed for the dislocation segments A and C (on scheme (*c*)) when exchanging entrance and exit surfaces; crystal-to-film distance $L \approx 50$ cm; Ge crystal, 220 reflection ($\lambda = 0.19$ Å, 65 keV, $\mu t = 0.24$). (*d*) Dislocation width as a function of L for the A and C segments (from Zontone *et al.* (1996)).

beam divergence, the direct image width of an edge dislocation may be observed to change with variations of the sample-to-film distance. This was assigned to the change in beam divergence induced by the defect through orientation contrast. They concluded that the image width of an edge dislocation is sensitive to the sign of the Burgers vector $\boldsymbol{b}$. Unfortunately, problems with stability prevented the actual study of these effects in more detail, and this pioneering work remained unique until the ESRF machine was ready.

The first diffraction topographic experiments performed at the ESRF therefore included the investigation of the variation of the image of dislocations, with a substantial edge component, as a function of the crystal orientation and sample-to-film distance. Figure 1*a*, *b* shows the images of a dislocation in a $(\bar{1}10)$ platelet-shaped germanium crystal, 0.325 mm thick, composed of three segments running

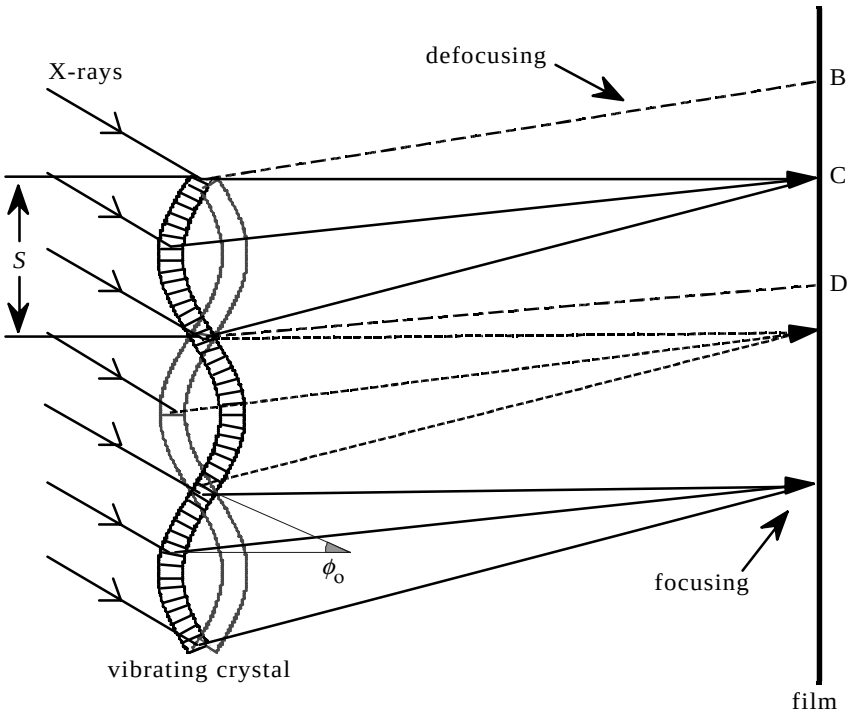

Figure 2. Illustration of the membrane-type vibration under magnetoacoustic excitation in $FeBO_3$: each segment S acts as a focusing lens periodically in time; the maximal rotation of the planes is indicated by ϕ_0.

along [111], [110] and [11$\bar{1}$], with Burgers vector $\boldsymbol{b}$ 1/2[110], obtained by interchanging the entrance and exit surfaces for the X-ray beam. The contrast of the dislocations is expected to be predominantly produced by the 'direct' image mechanism, because at the energy used (65 keV) the absorption is very low ($\mu t = 0.24$). The contrast of segments A and C (figure 1*c*) changes from simple to double, and vice versa. This corresponds to local orientation contrast, because the edge component of $\boldsymbol{b}$ changes sign with respect to the dislocation line when going from A to C, in such a way that the plane's curvature in the dislocation neighbourhood produces either focusing or defocusing. Figure 1*d* shows the evolution of the width of the images of segments A and C as a function of the sample-to-film distance L. It allows a complete determination, not only of the orientation, but also of the sign and modulus, of the Burgers vector (Zontone *et al*. 1996).

(*b*) *Visualizing magnetoelastic resonances in the MHz range in iron borate*

The application of an AC magnetic field on a thin crystal of iron borate $FeBO_3$, a weak ferromagnet with strong magnetoelastic coupling, induces, at certain frequencies, a membrane-like vibration. White-beam projection topographs were recorded on a very good quality (111) single crystal plate, 50 μm thick, excited into elastic resonance by a 1.3 MHz AC magnetic field superimposed on a small perpendicular DC field, both in-plane. The vibration of the magnetic moments induces standing

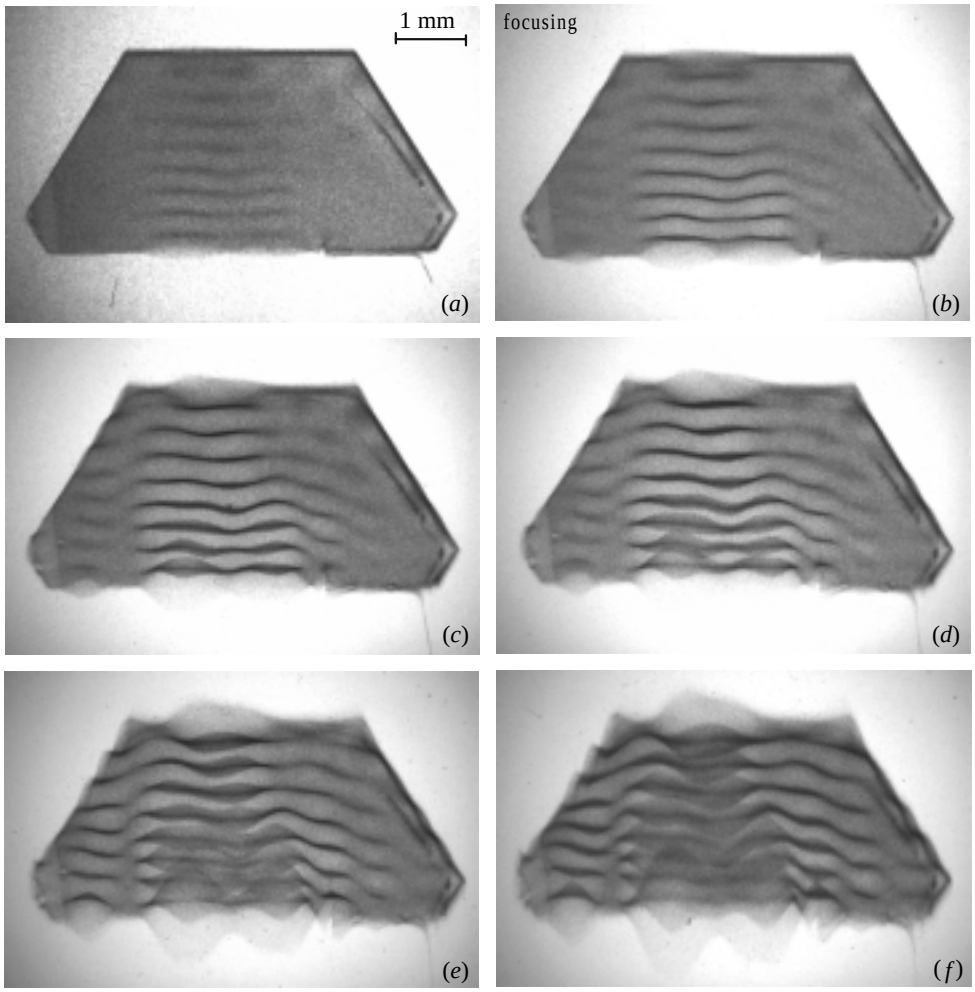

Figure 3. White-beam topographs of the $1\bar{2}1$ reflection, $FeBO_3$ crystal, as a function of the sample-to-film distance: (*a*) 19.5 cm, (*b*) 41 cm, (*c*) 55 cm, (*d*) 95 cm, (*e*) 114 cm, (*f*) 152 cm. The resonance pattern clearly reveals a focal distance of *ca.* 41 cm for the main resonant mode.

acoustic waves. In this imaging mode, the predominant effect is that of lattice plane rotation, with maximum amplitude ϕ_0 (figure 2). The application of the magnetic field is associated, in this case, with a nearly constant integrated intensity (less than 2% increase). But a membrane-type vibration leads to focusing of different components of the beam, as shown in figure 2 (with focal length varying periodically with time). Figure 3 shows some of the results obtained from one topograph as the sample–film distance L, for a given rotation amplitude ϕ_0, was varied. A formal theoretical description shows that the relevant parameter is the product $L\phi_0$ (Matsouli *et al*. 1998).

Such an experiment gives access to the main characteristics of the vibration: amplitude (*ca.* 50 nm), shape, polarization, wavelength and sound velocity ($4.5\,\mathrm{km\,s^{-1}}$) (Matsouli *et al*. 1998, 1999). In addition, this effect could be used to obtain a high-

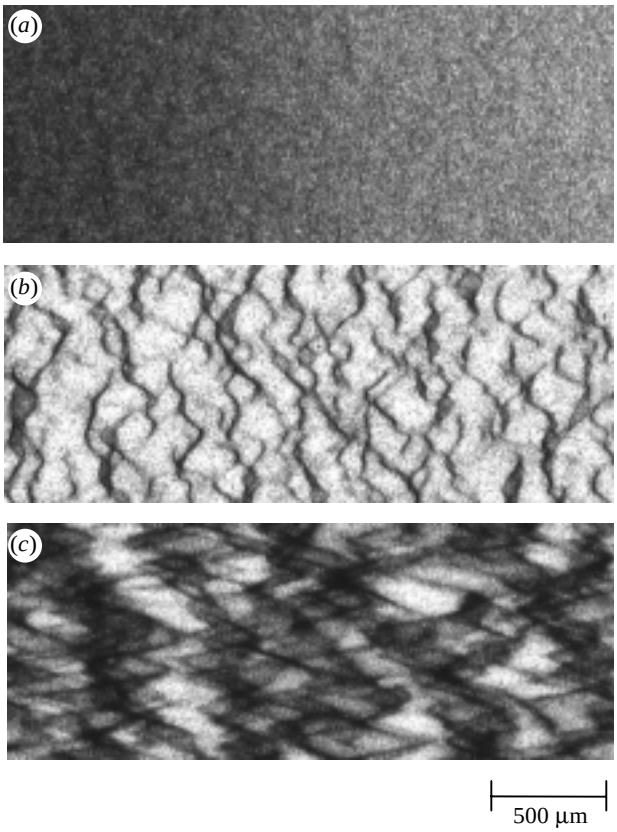

Figure 4. Series of white-beam topographs of the 022 layer reflection, of a wafer-bonded sample with a 15.4 µm Si layer, a 0.9 µm SiO_2 layer on a Si substrate, as a function of the sample-to-film distance: (*a*) 8 cm, (*b*) 40 cm, (*c*) 150 cm. The focusing distance is *ca.* 40 cm.

frequency, pulsed, 'monochromatic' and focused X-ray beam, or to study the variation of the sound velocity with the applied magnetic field, which remains a puzzling topic (Wettling & Jantz 1980).

(*c*) *Quantitative estimation of deformation in wafer-bonded samples*

The silicon-on-insulator (SOI) technology is an alternative method compared with conventional silicon technology for low power and low voltage applications. One of the promising, fast-progressing methods to produce SOI wafers is that of wafer bonding. It basically consists of the connection of a seed wafer (e.g. silicon) with one oxidized surface and a silicon handle wafer by directly contacting them. After thinning the handle wafer, the resulting SOI wafer displays the structure: thin silicon layer—silicon oxide—(silicon) substrate. Since the wafer surfaces are never perfectly smooth, the bonding process has to deform each wafer in order to achieve conformity of the two surfaces. In this way the lattice planes close to the bonding interface are deformed. This resembles to some degree the situation of the previous example of the vibrating plate, but now in a static case. The resulting long-range deformations may be easily detected by X-ray topography (see, for example, Maszara *et al.*

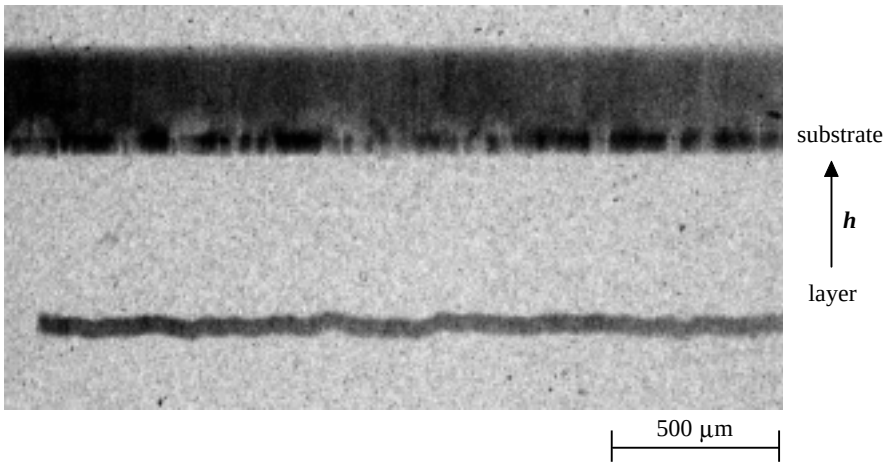

Figure 5. White-beam section topographs of a wafer-bonded sample with a 10.4 µm Si layer, showing a substrate and a layer reflection, 022 reflection, $\lambda \approx 0.04$ nm.

1991). Using white-beam topography (with an extended and/or a limited beam) and the new parameter, crystal-to-detector distance, it is possible to provide a detailed analysis of the contrast mechanism and above all a quantitative estimation of the deformations (Härtwig *et al*. 1999). Figure 4 shows a series of topographs taken for different distances. For small distances the wavy contrast disappears. This indicates that the contrast formation mechanism is orientation contrast (and not extinction contrast with changing integrated reflectivity). In a narrow range of distances a focusing effect is visible (figure 4*b*). Using this distance and the dominant spatial frequency of the contrast pattern (of the order of 200 µm) it is possible to estimate the maximum inclination of the lattice planes (of the order of 10 arc seconds) and the approximate amplitude of the deformation (of the order of 1.5 nm). Those results may be confirmed by other topographic methods, like, for example, white-beam section topography. Figure 5 shows an example where simultaneously a substrate and a layer image are visible. The wavy shape of the layer image is produced by the local change of the reflected beam direction due to the local misorientation of the reflecting lattice planes. The strongest lattice plane inclination may be estimated to be 30 arc seconds for this special sample, simply from the maximum amplitude within the image and the film-to-sample distance.

(*d*) *Probing symmetry: the low-temperature phase of magnetite*

Magnetite Fe_3O_4 is cubic above its Curie point, a ferrimagnet at room temperature, and exhibits at 120 K a transition affecting its electric and magnetic properties. Below this Verwey transition, the crystal symmetry is somewhat controversial. X-ray diffractometry indicates monoclinic symmetry (Yoshida & Iida 1979) while macroscopic measurements, especially of the magnetoelectric effect, involving ferroelectricity coupled with ferrimagnetism, suggest triclinic (Miyamoto 1994; Siratori *et al*. 1979) symmetry. In either case, it is clear that a single crystal should split into many domains or twins, and that information about these domains could provide indication of the symmetry.

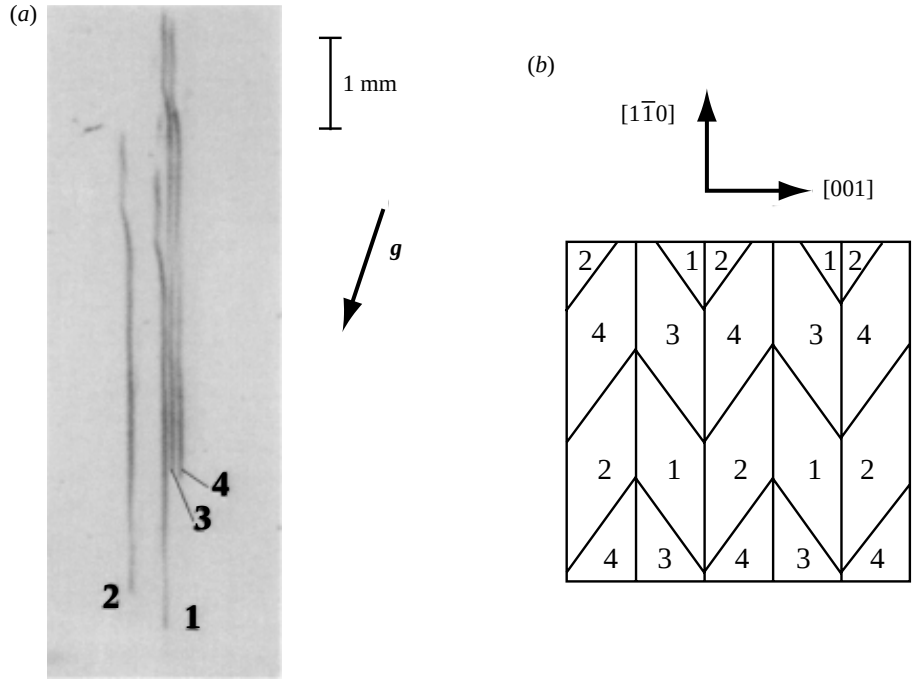

Figure 6. Magnetite crystal cooled to low temperature ($T = 20$ K) under a magnetic field applied along [001]; white-beam section topograph ($\bar{5}\bar{9}\bar{3}$ reflection, $\lambda = 0.3$ Å, $\mu t \approx 1$) and corresponding model of the domains present in the sample.

The domain structure was followed across the transition, using white-beam topography, in a sample with $(1\bar{1}0)$ surface and size $5 \times 7 \times 0.8\,\mathrm{mm}^3$, cut out of a crystal grown by the Bridgman technique, carefully polished using a mechano-chemical method. The least complicated situation prevailed, as expected, when the transition was passed in a magnetic field favouring one of the easy $\langle 001 \rangle$ magnetization directions, or the easy directions nearest [001]. Even then, however, so many domains were superimposed on any projection topograph that, contrary to standard usage, this provided no overall view. White-beam section topographs, in which the beam width was reduced to 20 μm, provided clues on the coexisting domains, their shape and arrangement.

Figure 6*a* shows a typical result, corresponding to one white-beam section topograph, obtained with a specimen–film distance of 40 cm. It is to be compared with the single straight line a single domain would yield. Unravelling these data involved first the determination of matching lines, associated with adjacent domains in the specimen, from their position and relative extension. The geometric splitting of the corresponding lines, due to the relative rotation of the lattice planes, was measured for a number of Laue spots. They were then compared with the result of calculations. The outcome (Medrano *et al*. 1999) is a plausible model, shown in figure 6*b*, of monoclinic domains, with all walls satisfying the conditions of no magnetic or electric charge distributions, and no long-range elastic stress. Supplementary contrast is observed, and is the first unambiguous evidence of extra distortions associated with triclinic symmetry.

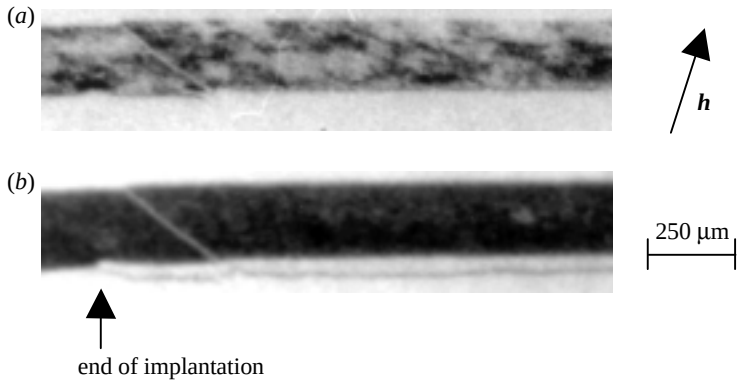

Figure 7. Section topographs, $\bar{2}016$ reflection, implanted Y-cut $LiNbO_3$, $\mu t = 1.2$ ($\lambda = 0.23$ Å, $\boldsymbol{h}$ is the projection of the diffraction vector on the film). Electric field (*a*) $E = 0$, (*b*) $E = -17$ kV.

The ability to vary the sample–film distance, to obtain high sensitivity to lattice plane rotation at relatively large distances, and to confirm the assignment of matching elements at smaller distances, proved essential in this work.

(*e*) *Characterizing a buried implanted layer region in an* $LiNbO_3$ *crystal*

Lithium niobate ($LiNbO_3$) displays a number of large-magnitude physical effects, which make it an attractive material for applications such as guided-wave optics. Implantation of $LiNbO_3$ by high energy (of the order of megaelectronvolts) light ions such as hydrogen or helium has the effect of considerably lowering the refractive index in the implanted region, while the refractive index of the layer only traversed by the implanted ions generally remains approximately the same as in the bulk. The region of lower refractive index (implanted layer, thickness in the micrometre range) can thus act as the boundary of a waveguiding area (the traversed layer, thickness up to 15 µm).

Section topographs were used to investigate these layers, which appeared to be very weakly misoriented (*ca.* 1 arc seconds) with respect to the bulk. Figure 7 shows section topographs of a Y-cut $LiNbO_3$ crystal, without field and under an electric field applied along the Y-axis. The image of the layer associated with the implantation moves either way relative to the image of the bulk when changing the polarity of the applied field. The distance of the image of this layer with respect to the bulk image, i.e. its misorientation, is proportional to the field and appears to be strongly related to the piezoelectric effect. Chemical etching and topographic experiments indicate that the observed layer corresponds to a region of inverse polarization with respect to the bulk, several micrometres thick, located at the level of the implanted layer (Rejmánková *et al.* 1996).

3. ‘Coherence’-related experiments

The small angular size of the X-ray source leads to a high spatial coherence of the photon beam. The transverse coherence length, $l_c = \lambda D/(2s)$ (where λ is the wavelength, s is the source size, and D is the source-to-sample distance), is, at ID19

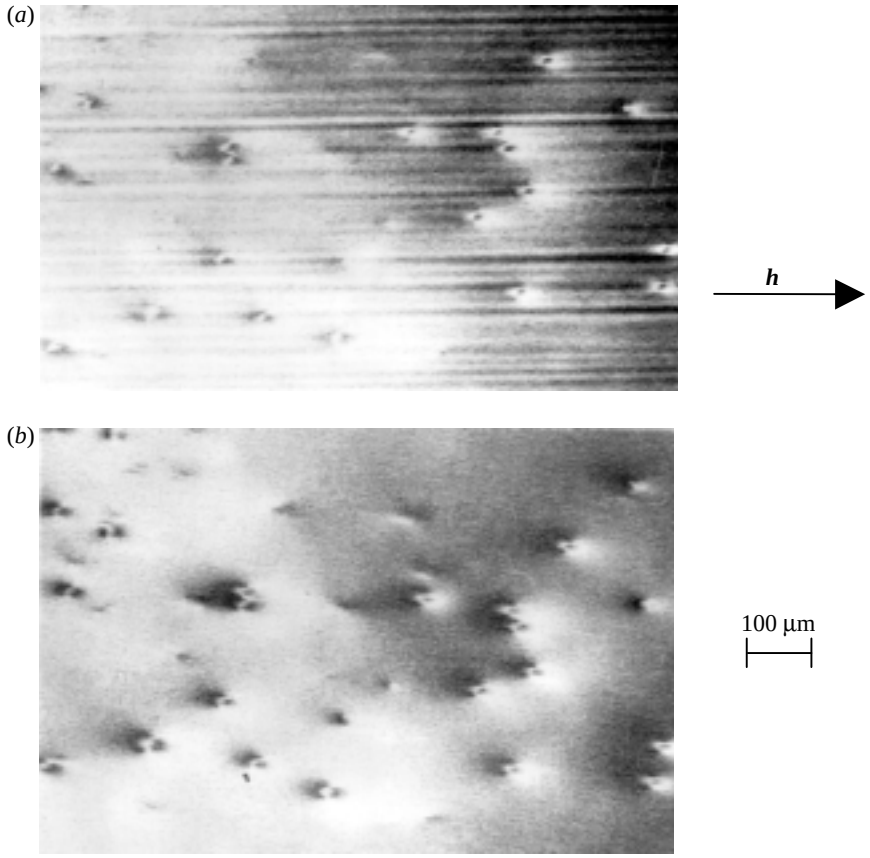

Figure 8. 022 topographs ($\lambda = 0.37$ Å, $E = 33.5$ keV) of a SIMOX sample (540 µm Si substrate + 0.4 µm SiO_2 amorphous layer + 10 µm epitaxial Si capping layer) (*a*) with no random phase screen (RPS) and (*b*) with a 2 mm thick ash wood RPS. Dislocations in the top layer are visible in (*a*) as well as corrugations on a beryllium window. The use of the RPS in (*b*) blurs completely the phase image of the beryllium window and affects only slightly the image of the dislocations (from Cloetens *et al.* (1996)).

and for $\lambda \approx 1$ Å, *ca.* 0.1 mm. This is the basis of all the coherence-related topographic experiments shown here as examples of the new possibilities.

(*a*) *Coherence and diffraction topography: general features*

Such a coherent beam produces phase images, whether they are wanted or not, of objects present in the X-ray path (beryllium windows, dust particles, etc.) that are nearly non-absorbing at the photon energies used. Their images are due to the spatial variations of the phase of the transmitted beam, associated with local variations in optical path length. Such phase images can disturb the observation and interpretation of the topographic ones, as shown in figure 8*a* where the horizontal striations correspond to small variations in thickness (*ca.* 5 µm) of a 500 µm thick beryllium window. It is mandatory, to avoid these effects, to use clean slits for section topography (which requires a confinement of the slits within a controlled atmosphere,

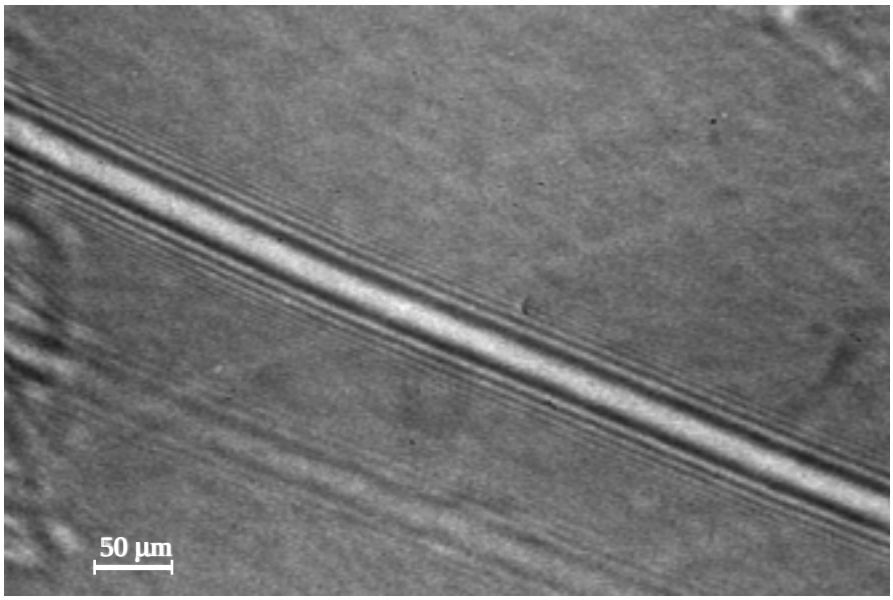

Figure 9. Phase-contrast image of a surface scratch on a (111) silicon crystal; Bragg symmetrical setting; sample-to-film distance 92 cm ($\lambda = 0.53$ Å, $E = 21$ keV). The fringes associated with the edge of the crystal are also visible.

because the electrostatic effects associated with the X-ray beam itself can attract dust particles) and carefully polished filters and windows (Espeso *et al*. 1998). If this is not possible, a random phase plate, which provides an effective way of tailoring the beam divergence, can be added to obtain better topographic results, as shown in figure 8*b* (Cloetens *et al*. 1996).

The usual requirement in diffraction topography is that the surfaces of the investigated crystal (and/or monochromator) should be strain free; no specific demand is made on their flatness. This is no longer true when dealing with high quality crystals and using a coherent X-ray beam. Figure 9 shows the image of a surface scratch, which is mainly a phase contrast image, the direct image component being very weak (Baruchel 1996). This type of contrast was recently analysed by Kuznetsov and co-workers (Kuznetsov *et al*. 1999).

(*b*) *Retrieving the phase of the structure factor from diffraction topographic images with a coherent beam*

When X-ray diffraction topography is performed on a crystal that is subdivided into ferroelectric domains, or inversion twins, the phase of the diffracted beam leaving the crystal is expected to change from one domain to the next. This phase is that of the structure factor of the reflection used, which can be described as hkl in domain I and as $\bar{h}\bar{k}\bar{l}$ in the inverted structure of domain II. If the domain distribution is periodic, the situation is identical to the Talbot effect in simple transmission, except that now Fresnel interference will occur between parts of the Bragg-diffracted wave instead of the simply transmitted wave.

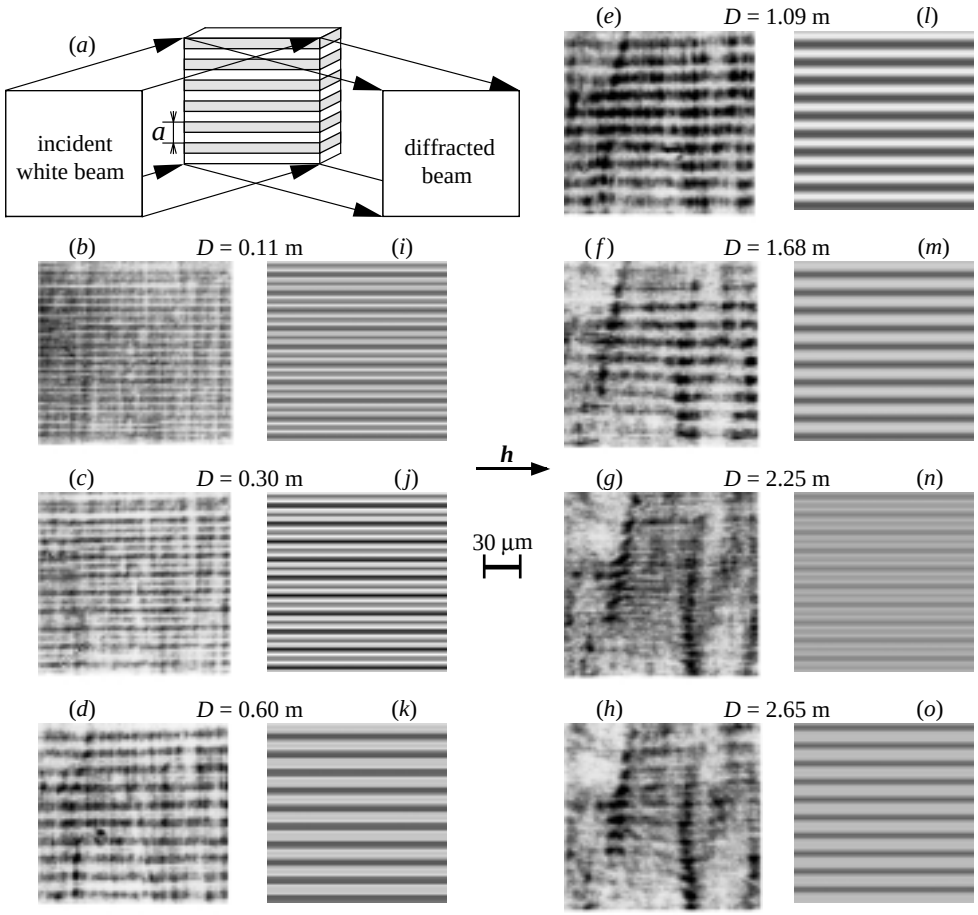

Figure 10. Poled Z-cut $LiNbO_3$: (*a*) scheme of the experiment geometry; (*b*)–(*h*) white-beam topographs ($\lambda = 1$ Å), 006 reflection, as a function of the sample-to-film distance; (*i*)–(*o*) corresponding simulations (see text).

The Talbot effect of self-imaging of periodic objects, discovered in 1836 for visible light (Talbot 1836), was revisited with hard X-rays recently (Cloetens *et al*. 1997*a*). In a coherent beam, the contrast varies with the specimen–detector distance L, with a period, the Talbot distance, $D_{\mathrm{T}} = 2p^2/\lambda$, where p is the period in the object. In the case of a phase object, no contrast is expected immediately behind the object. It increases up to a maximum and vanishes again at a distance $D_{\mathrm{T}}/2$. At a distance $D_{\mathrm{T}}/4$ the visibility $((I_{\max} - I_{\min})/I_{\mathrm{mean}})$ is given by $2\sin(\Delta\varphi)$ and a simple relationship exists between the phase-object and the image (Cloetens *et al*. 1997*a*).

Measuring the variation of contrast with L can provide the value of the difference in phase between the domains, i.e. the difference in structure factor phase $\Delta\varphi = |\varphi_{\mathrm{I}} - \varphi_{\mathrm{II}}|$ for the Friedel pair (Rejmánková-Pernot *et al*. 1998).

Figure 10 shows a schematic drawing of the experimental set-up, and the images recorded at several sample-to-film distances L, as well as their simulations. It is important to note that the relative difference of the moduli $|F_{hkl}|$ and $|F_{\bar{h}\bar{k}\bar{l}}|$, for the 006 reflection shown in figure 10, is less than 1% and therefore cannot explain

the observed contrast. F_{hkl} and $F_{\bar{h}\bar{k}\bar{l}}$ differ, however, substantially in their phases. The value estimated, from a set of simulations, for $\Delta\varphi$ is 140° (±5°), in very good agreement with the value of 141° calculated from the published structure. The displacement of the niobium ion, 54 pm along the *c*-axis, is the main contribution to the phase-shift between the structure factors of neighbouring domains.

This approach opens the way to the investigation of tiny variations of the atomic positions as a function of an external parameter.

4. Conclusion

The experiments described illustrate some of the new possibilities for diffraction topography at third generation SR machines. They rest on the small angular size of the source as seen from the sample.

The good spatial resolution retained even when setting the film far from the sample is important in that it allows the use of the sample-to-detector distance as an additional tool that can help understanding the behaviour of a crystal. This was used to characterize vibrating crystals or domains. The large spatial transverse coherence length (*ca.* 100 μm) of the beam reaching the sample has been applied to the determination of the phase difference between the structure factors corresponding to opposite ferroelectric domains in $LiNbO_3$. This combination of phase and diffraction images provides a new possibility for investigating features associated with phase jumps in crystals.

The results described in the present paper originate from the common work of several scientists, from the Topography/Imaging ID19 group of the ESRF. We are happy to thank these colleagues for their friendly and efficient collaboration. More particularly, among them, we acknowledge José Espeso (now at the University of Cantabria, Santander, Spain), Jean-Pierre Guigay, Vladimir Kvardakov (Kurchatov Institute, Moscow, Russia), Lucia Mancini (now at the Lamel, Bologna, Italy), Ioanna Matsouli, Carlos Medrano (now at the Escuela Universitaria Politécnica, Teruel, Spain), Etienne and Petra Pernot, and Federico Zontone.

References

Baruchel, J. 1996 In *X-ray and neutron dynamical diffraction: theory and applications* (ed. A. Authier, S. Lagomarsino & B. K. Tanner), pp. 399–409. New York: Plenum Press.

Baruchel, J., Epelboin, Y., Gastaldi, J., Härtwig, J., Kulda, J., Rejmánková, P., Schlenker, M. & Zontone, F. 1994 First topographic results at the European Synchrotron Radiation Facility. *Physica Status Solidi* A **141**, 59–69.

Cloetens, P., Barrett, R., Baruchel, J., Guigay, J. P. & Schlenker, M. 1996 Phase objects in synchrotron radiation hard X-ray imaging. *J. Phys.* D **29**, 133–146.

Cloetens, P., Guigay, J. P., De Martino, C., Baruchel, J. & Schlenker, M. 1997*a* Fractional Talbot imaging of phase gratings with hard X-rays. *Opt. Lett.* **22**, 1059–1061.

Cloetens, P., Pateyron-Salome, M., Buffiere, J. Y., Peix, G., Baruchel, J., Peyrin, F. & Schlenker, M. 1997*b* Observation of microstructure and damage in materials by phase sensitive radiography and tomography. *J. Appl. Phys.* **81**, 5878–5886.

Cloetens, P., Ludwig, W., Baruchel, J., Guigay, J. P., Rejmánková-Pernot, P., Salome, M., Schlenker, M., Buffiere, J. Y., Maire, E. & Peix, G. 1999 Hard X-ray phase imaging using simple propagation of a coherent synchrotron radiation beam. *J. Phys.* D **32**, A145–A151.

Espeso, J. I., Cloetens, P., Baruchel, J., Härtwig, J., Mairs, T., Biasci, J. C., Marot, G., Salome-Pateyron, M. & Schlenker, M. 1998 Conserving the coherence and uniformity of third-generation synchrotron beams: the case of ID19, a 'long' beamline at ESRF. *J. Synchrotron Rad.* **5**, 1243–1249.

Härtwig, J., Köhler, S., Ludwig, W., Moriceau, H., Ohler, M. & Prieur, E. 1999 (In preparation.)

Kuznetsov, S., Snigireva, I., Souvorov, A. & Snigirev, A. 1999 New features of X-ray Bragg diffraction topography with coherent illumination. *Physica Status Solidi* A **172**, 3–13.

Lang, A. L., Kowalski, G., Makepeace, A. L. W., Moore, M. & Clockson, S. G. 1987 Single-slit diffraction patterns of sub-nanometre-wavelength synchrotron radiation. *J. Phys.* D **20**, 541–544.

Mancini, L., Reinier, E., Cloetens, P., Gastaldi, J., Härtwig, J., Schlenker, M. & Baruchel, J. 1998 Investigation of defects in AlPdMn icosahedral quasicrystals by combined synchrotron X-ray topography and phase radiography. *Phil. Mag.* A **78**, 1175–1174.

Maszara, W. P., Jiang, B. L., Yamada, A., Rozgonyi, G. A., Baumgart, H. & De Kock, A. J. R. 1991 Role of surface morphology in wafer bonding. *J. Appl. Phys.* **69**, 257–260.

Matsouli, I., Kvardakov, V., Espeso, J. I., Chabert, L. & Baruchel, J. 1998 A study of the X-ray focusing effect of a magneto-acoustically excited $FeBO_3$ crystal using synchrotron radiation diffraction imaging. *J. Phys.* D **31**, 1478–1486.

Matsouli, I., Pernot, E., Baruchel, J., Kvardakov, V., Chabert, L. & Palmer, S. B. 1999 Section and stroboscopic diffraction imaging of the magneto-acoustic vibrations in $FeBO_3$ by synchrotron radiation. *J. Phys.* D. (In the press.)

Medrano, C., Schlenker, M., Baruchel, J., Espeso, J. I. & Miyamoto, Y. 1999 Domains in the low temperature phase of magnetite from synchrotron radiation X-ray topographs. *Phys. Rev.* B **59**, 1185–1195.

Miyamoto, Y. 1994 Magneto-electric measurements of magnetite (Fe_3O_4) at low temperatures. *Ferroelectrics* **161**, 117–123.

Raven, C., Snigirev, A., Snigireva, I., Spanne, P., Souvorov, A. & Kohn, V. 1996 Phase-contrast micro-tomography with coherent high-energy synchrotron X-rays. *Appl. Phys. Lett.* **69**, 1826–1828.

Rejmánková, P., Baruchel, J. & Moretti, P. 1996 Investigation of hydrogen implanted $LiNbO_3$ under a DC electric field by synchrotron radiation. *Physica* B **226**, 293–303.

Rejmánková-Pernot, P., Cloetens, P., Baruchel, J., Guigay, J. P. & Moretti, P. 1998 Phase retrieval by combined Bragg and Fresnel X-ray diffraction imaging. *Phys. Rev. Lett.* **81**, 3435–3438.

Siratori, K., Kita, E., Kaji, G., Tasaki, A., Kimura, S., Shindo, I. & Kohn, K. 1979 Magneto-electric effect of Fe_3O_4 at 77 K. I. Crystal symmetry. *J. Phys. Soc. Japan* **47**, 1779–1787.

Snigirev, A., Snigireva, I., Kohn, V. G., Kuznetzov, S. M. & Schelokov, I. 1995 On the possibilities of X-ray phase contrast micro-imaging by coherent high-energy synchrotron radiation. *Rev. Sci. Instrum.* **66**, 5486–5492.

Talbot, H. F. 1836 Facts relating to optical science. IV. *Lond. Edinb. Phil. Mag. J. Sci.* (3rd Series) **9**, 401–407.

Tanner, B. K., Midgley, D. & Safa, M. 1977 Dislocation contrast in X-ray synchrotron topographs. *J. Appl. Cryst.* **10**, 281–286.

Wettling, W. & Jantz, W. 1980 Magnetically tuneable sound velocity in iron borate. *J. Appl. Phys.* **23**, 195–198.

Yoshida, J. & Iida, S. 1979 X-ray study of the phase transition in magnetite. *J. Phys. Soc. Japan* **47**, 1627–1633.

Zontone, F., Mancini, L., Baruchel, J., Härtwig, J. & Epelboin, Y. 1996 New features of dislocation images in third-generation synchrotron radiation topographs. *J. Synchrotron Rad.* **3**, 173–184.